

Sky reconstruction for the Tianlai cylinder array

Jiao Zhang^{1,2,3}, Shifan Zuo^{1,3}, Reza Ansari², Xuelei Chen^{1,3,4}, Yichao Li^{1,3}, Fengquan Wu^{1,3}, Jean-Eric Campagne², Christophe Magneville⁵

¹ Key Laboratory of Computational Astrophysics, National Astronomical Observatories, Chinese Academy of Sciences, Beijing 100012, China

² Université Paris-Sud, LAL, UMR 8607, F-91898 Orsay Cedex, France & CNRS/IN2P3, F-91405 Orsay, France

³ University of Chinese Academy of Sciences, Beijing 100049, China

⁴ Center for High Energy Physics, Peking University, Beijing 100871, China

⁵ CEA, DSM/IRFU, Centre d'Etudes de Saclay, F-91191 Gif-sur-Yvette, France

Abstract In this paper, we apply our sky map reconstruction method for transit type interferometers to the Tianlai cylinder array. The method is based on the spherical harmonic decomposition, and can be applied to cylindrical array as well as dish arrays and we can compute the instrument response, synthesised beam, transfer function and the noise power spectrum. We consider cylinder arrays with feed spacing larger than half wavelength, and as expected, we find that the arrays with regular spacing have grating lobes which produce spurious images in the reconstructed maps. We show that this problem can be overcome, using arrays with different feed spacing on each cylinder. We present the reconstructed maps, and study the performance in terms of noise power spectrum, transfer function and beams for both regular and irregular feed spacing configurations.

Key words: Cosmology: observation, HI intensity mapping; Method: transit telescope; map making

1 INTRODUCTION

The determination of the neutral hydrogen (HI) distribution from 21cm line observation is an important method to study the statistical properties of Large Scale Structures in the Universe. The intensity mapping technic is an efficient and economical way to map the universe using the (HI) 21cm emission, which is suitable for late time cosmological studies ($z \lesssim 3$), especially for constraining dark energy models through baryon acoustic oscillation (BAO) features (Peterson et al. 2006; Chang et al. 2008; Ansari et al. 2009; Ansari et al. 2012; Seo et al. 2010; Gong et al. 2011). Large wide-field and wide band radio telescopes would be needed to achieve rapidly the observation of large volumes of the universe. Several dedicated experiments are aimed at such surveys, including our own experiment Tianlai¹ (Chen 2012), as well as CHIME (Bandura et al. 2014), BINGO (Battye et al. 2013), HIRAX², and BAORadio³.

¹ <http://tianlai.bao.ac.cn>

² <http://www.acru.ukzn.ac.za/cosmosafari/wp-content/uploads/2014/08/Sievers.pdf>

³ <http://groups.lal.in2p3.fr/bao21cm>

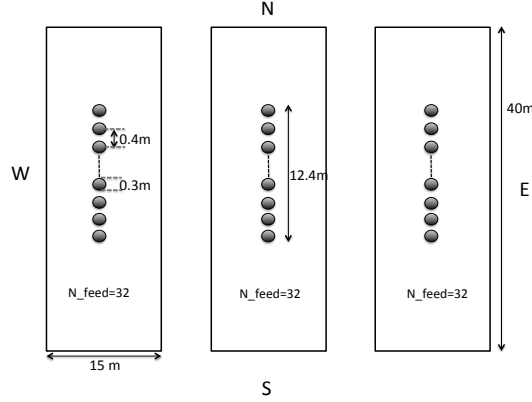


Fig. 1 Regular configuration of the cylinder array.

In transit mode intensity mapping surveys, the antennas are fixed on the ground during observation, it observes the sky as the Earth rotates. For the cylinder arrays such as Tianlai and CHIME, the instantaneous field of view is a strip of sky along the meridian, and sky patches of different right ascension pass through the field of view. As the telescopes do not need to track the celestial target, the mechanical structure of the telescope is very simple.

The Tianlai project is designed to survey the large scale structure by intensity mapping of the redshifted 21cm line, and to constrain dark energy models by baryon acoustic oscillation (BAO) measurement. As a first step, the current pathfinder experiment will test the basic principles and key technologies of the 21cm intensity mapping method. The Tianlai array is a wide band interferometer which features both a cylinder array and a dish array, installed at a radio quiet site ($44^{\circ}10'47''N, 91^{\circ}43'36''E$) in Hongliuxia, Balikun County, Xinjiang Autonomous Region in northwest China (Chen 2015). The construction of the Tianlai cylinder and dish pathfinder arrays have been completed at the end of 2015, the two arrays are now undergoing the commissioning process. The map making algorithm and its application to dish arrays has been presented in Zhang et al. (2016), heretofore referred to as **paper I**. In the present paper, we will focus on its application to the Tianlai pathfinder cylinder array.

The Tianlai cylinder pathfinder array has three adjacent cylindrical reflectors oriented in the North-South direction, each cylinder is 15 m wide and 40 m long. At present the cylinders are equipped with a total of 96 dual polarization receivers which do not cover the full length of the cylinders. In the future, the pathfinder instrument may be upgraded by simply adding more feed units and the associated electronics. The longer term plan is to expand the Tianlai array to full scale once the principle of intensity mapping is proven to work. The full scale Tianlai cylinder array would have a collecting area of $\sim (10^4 \text{ m})^2$, and $\sim 10^3$ receiver units. A forecast for its capability in measuring dark energy and constrain primordial non-Gaussianity can be found in Xu et al. (2015). In addition to the redshifted 21 cm intensity mapping observation, such surveys may also be used for other observations, such as 21cm absorber (Yu et al. 2014), fast radio burst (FRB) (Masui et al. 2015; Connor et al. 2016), and electromagnetic counter part of gravitational wave events (Feng et al. 2014).

The simplest arrangement of the existing 96 feeds is to have 32 feeds on each cylinder, regularly spaced so that on each cylinder the feeds form a uniformly spaced linear array. Two such configurations are considered here:

- Regular 1. The feed spacing is taken to be $d_{\text{sep}} = 0.4\text{m}$, which is about one wavelength at the observation frequency of 750 MHz. In this configuration, the feeds occupies only 12.4 m of the total 40 m length of the cylinder, as shown in Fig1.
- Regular 2. The feed spacing is taken to be $d_{\text{sep}} = 0.8\text{m}$, about twice the wavelength at the cylinder,

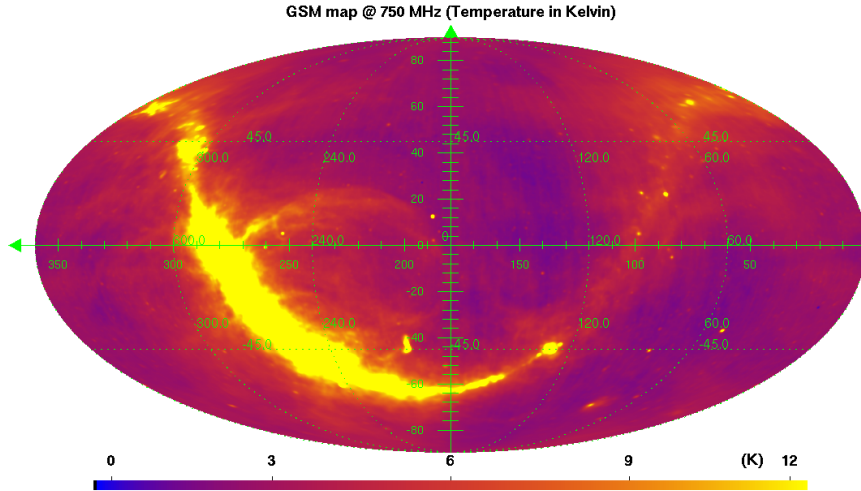


Fig. 2 GSM (Global Sky Model) map at 750 MHz, used as the true sky for the reconstruction with the Tianlai cylinder configuration.

One may also consider configurations with irregular positioning of the feeds to reduce grating lobes. In this paper we consider a very simple extension: on each cylinder the feeds still forms a uniform linear array, but the number of feeds and hence the spacing of the array is different on each cylinder. We have total 96 feeds at the present time. Marking the cylinders from East to West as cylinder1, cylinder2 and cylinder3 respectively, we consider the following configurations:

- Irregular 1. This is the first irregular cylinder array with number of feeds on each cylinder 31, 32 and 33 respectively. The feeds occupy 12.4 m along NS direction on each cylinder. The feed spacing would be $d_{\text{sep}} = 0.413m$ for cylinder1, $d_{\text{sep}} = 0.4m$ for cylinder2 and $d_{\text{sep}} = 0.388m$ for cylinder3.
- Irregular 2. This is the second irregular cylinder array with number of feeds on each cylinder 31, 32 and 33 respectively, but the feeds occupy 24.8 m along NS direction on each cylinder. The feed spacing would be $d_{\text{sep}} = 0.827m$ for cylinder1, $d_{\text{sep}} = 0.8m$ for cylinder2 and $d_{\text{sep}} = 0.775m$ for cylinder3 for this

To simulate the map making process, we use an input map based on the Global Sky Model (GSM) (de Oliveira-Costa et al. 2008), shown in Fig. 2. The map is obviously dominated by the radiation from the galactic plane, which is mostly synchrotron emission from galactic cosmic ray electrons. For the computations carried out in this work, we have used HEALPix (Górski et al. 2005) to pixellate the celestial sphere, with $n_{\text{side}} = 512$. In our spherical harmonics transformation we take $\ell_{\text{max}} = 1500$, which is sufficient for the angular resolution of Tianlai pathfinder cylinder array.

Below, we present in Sec. 2 a brief review of the spherical harmonic decomposition map making method. In Sec. 3 we discuss the grating lobe problem and spurious image for regular receivers layout. To resolve this problem, in Sec. 4 we study the case of irregular layouts listed above. We present our conclusion in section 5.

2 A BRIEF REVIEW OF SKY RECONSTRUCTION METHOD

In this section, we present briefly the map making method for transit interferometer array based on spherical harmonic decomposition. A more detailed presentation and comparison with the classical radio interferometry (tracking type surveys) can be found in paper I, as well as in Shaw et al. (2014). Unlike the frequently used tracking observations, it is more convenient to work in ground coordinates

in which the baselines of the array do not change in the transit observation. In this formalism, the visibilities recorded as a function of time correspond to observations of different parts of the sky. We separate the inversion problem into independent sub-systems using m-mode decomposition in spherical harmonics and we assume that the individual feed responses and array geometry are known. The sky emission intensity is $I(\hat{\mathbf{n}}) = \langle \mathbf{E}^*(\hat{\mathbf{n}}, t) \cdot \mathbf{E}(\hat{\mathbf{n}}, t) \rangle_t$, where $\hat{\mathbf{n}} = (\alpha, \delta)$ denotes the sky direction, and the receivers are sensitive to the sky emission complex amplitudes $\mathbf{E}(\hat{\mathbf{n}})$. A single receiving element can be characterized by its angular complex response $D(\hat{\mathbf{n}})$ and its position \mathbf{r} , the output of element j is

$$s_j(t) = \iint d\hat{\mathbf{n}} D_j(\hat{\mathbf{n}}, t) E(\hat{\mathbf{n}}, t) e^{i\mathbf{k} \cdot \mathbf{r}_j} \quad (1)$$

The Visibility $V_{ij} = \langle s_i^* s_j \rangle_t$ is the short time average of the cross correlation of the outputs of a pair of antennae or feeds s_i, s_j , located at positions $\mathbf{r}_i, \mathbf{r}_j$ with $\mathbf{r}_{ij} \equiv \mathbf{r}_j - \mathbf{r}_i$. As the emission of the different sky directions are incoherent, only the wave from the same sky direction are correlated, and the integration yields the interferometer equation

$$V_{ij} = \iint D_i^*(\hat{\mathbf{n}}) D_j(\hat{\mathbf{n}}) I(\hat{\mathbf{n}}) e^{i\mathbf{k} \cdot \mathbf{b}_{ij}} d\hat{\mathbf{n}} \quad (2)$$

$$= \iint L_{ij}(\hat{\mathbf{n}}) I(\hat{\mathbf{n}}) d\hat{\mathbf{n}}, \quad (3)$$

In a transit instrument, visibilities are measured as a function of time or right ascension, with the beam response $L_{ij}(\hat{\mathbf{n}})$ changing due to earth rotation. In discrete form, including the noise contribution and gathering visibility measurement from all baselines and from all times into a vector, we can write the full measurement equation in matrix form:

$$[\mathbf{V}] = [\mathbf{L}][\mathbf{I}] + [n]. \quad (4)$$

where we have used the square brackets to emphasis these are vectors and matrices, and the time ordered visibility data $[\mathbf{V}]$ is linearly related to the sky intensity of different directions \mathbf{I} by the time dependent beam response represented as the matrix $[\mathbf{L}]$. The interferometer array map-making is to solve this system and reconstruct \mathbf{I} from the observed time ordered visibility data.

We expand the sky intensity and beam response into spherical harmonics,

$$I(\hat{\mathbf{n}}) = \sum_{\ell=0}^{+\infty} \sum_{m=-\ell}^{+\ell} \mathcal{I}_{\ell,m} Y_{\ell,m}(\hat{\mathbf{n}}), \quad (5)$$

$$L_{ij}(\hat{\mathbf{n}}) = \sum_{\ell=0}^{+\infty} \sum_{m=-\ell}^{+\ell} \mathcal{L}_{\ell,m} Y_{\ell,m}(\hat{\mathbf{n}}). \quad (6)$$

where (θ, ϕ) are the polar coordinates, $\theta = 90^\circ - \delta$, $\phi = \alpha$. $Y_{\ell,m}(\hat{\mathbf{n}})$ are the spherical harmonic functions. Then the visibilities can also be written as a summation of spherical harmonic modes,

$$V_{ij} = \sum_{\ell,m} (-1)^m \mathcal{I}_{\ell,m} \mathcal{L}_{\ell,-m}$$

For the transit interferometer array, the effect of the Earth rotation is that the beam $L_{ij}(\hat{\mathbf{n}})$ has a constant drift along the right ascension direction, with the offset angle given by $\alpha_p(t) = \alpha_0 + \Omega_e t$, where Ω_e is angular rotation rate of the Earth, so that

$$L_{ij}(\hat{\mathbf{n}}, t) = L_{ij}((\theta, \varphi), t) = L_{ij}(\theta, \varphi - \alpha_p(t)). \quad (7)$$

The spherical harmonics coefficients of the rotated/shifted beams can be written as $\mathcal{L}_{\ell,m}(t_k) = \mathcal{L}_{\ell,m} e^{-im\alpha_p(t)}$. The recorded visibilities as a function of α_p are then

$$V_{ij}(\alpha_p) = \sum_{m=-\infty}^{+\infty} \sum_{\ell=|m|}^{+\infty} (-1)^m \mathcal{I}_{\ell,m} \mathcal{L}_{\ell,-m} e^{im\alpha_p} \quad (8)$$

We recognise the expression as a Fourier series for the periodic function $V_{ij}(\alpha_p)$; the corresponding Fourier coefficients $\tilde{V}_{ij}(m)$, computed from a set of regularly time sampled visibility measurements is

$$\tilde{V}_{ij}(m) = (-1)^m \sum_{\ell=|m|}^{+\ell_{max}} \mathcal{I}_{\ell,m} \mathcal{L}_{\ell,-m} + \text{noise} \quad (9)$$

Grouping m -mode visibilities from all baselines in a vector and using matrix notation, we can write the measurement equation for each m -mode as:

$$\left[\tilde{V}_{ij} \right]_m = \mathbf{L}_{ij,m} \times [\mathcal{I}(\ell)]_m + [\tilde{n}_{ij}]_m \quad (10)$$

or putting all baselines of the array together,

$$\left[\tilde{V} \right]_m = \mathbf{L}_m \times [\mathcal{I}(\ell)]_m + [\tilde{\mathbf{n}}]_m \quad (11)$$

Comparing with Eq.(4), the full linear system is decomposed into a set of $m_{max} = \ell_{max}$ independent smaller system, one for each m -mode, which have much smaller dimensions ($n_{baseline} \times \ell_{max}$) and are thus much easier to solve numerically.

We assume that the noise on visibility measurement follows a gaussian random process, with variance $\mathbf{N} = \langle nn^\dagger \rangle$. Using maximum likelihood method, the solution of observed sky is given by

$$\left[\hat{\mathcal{I}} \right]_m = \mathbf{L}_m^{-1} [\tilde{V}]_m \quad (12)$$

where \mathbf{L}_m^{-1} denotes the noise weighted pseudo-inverse matrix of \mathbf{L}_m . This can be computed by using the singular-value-decomposition (SVD) method: any $m \times n$ matrix \mathbf{A} can be decomposed as $\mathbf{A} = \mathbf{U}\mathbf{\Sigma}\mathbf{Q}^\dagger$, where \mathbf{U} and \mathbf{Q} are $m \times m$ and $n \times n$ unitary matrices, and $\mathbf{\Sigma}$ is an $m \times n$ rectangular diagonal matrix, i.e. all non-diagonal elements are zero, with non-negative real numbers on the diagonal. The pseudo-inverse is given by

$$\tilde{\mathbf{A}}^{-1} = \mathbf{Q}\tilde{\mathbf{\Sigma}}^{-1}\mathbf{U}^\dagger \quad (13)$$

where $\tilde{\mathbf{\Sigma}}^{-1}$ is obtained by replacing all diagonal elements e_{ii} above certain threshold value by their reciprocal $1/e_{ii}$, while setting the other elements zero. For details of computing the pseudo-inverse, see e.g. Barata & Hussein (2012).

Substitute Eq. (11) to Eq. (12), and neglecting the noise, we have $\hat{\mathcal{I}} = \mathcal{R}\mathcal{I}$, where \mathcal{R} denotes the reconstruction or response matrix, which relates the reconstructed sky to the original sky. In the spherical harmonics representation, the m -mode reconstruction matrix is $\mathbf{R}_m \equiv \tilde{\mathbf{L}}_m^{-1}\mathbf{L}_m$. Ideally, if $\mathbf{R}_m = \mathbf{I}$ then the reconstruction for the m -mode is completely accurate. In practice, the reconstruction is usually not fully accurate.

For each given m , the different ℓ coefficients are correlated, the physical measurement data is a mix of different ℓ mode contributions. We can define the compressed response matrix \mathbf{R} by extracting the diagonal terms from individual \mathbf{R}_m matrices:

$$\mathbf{R}(\ell, m) = \mathbf{R}_m(\ell, \ell)$$

Obviously, the $\mathbf{R}(\ell, m)$ do not describe fully the reconstruction in the (ℓ, m) plane and the original \mathbf{R}_m matrices are needed. However, the $\mathbf{R}(\ell, m)$ matrix can give some idea of how well an (ℓ, m) mode is measured with a given array configuration, so it can help us to compare the performance of different configurations.

If we consider the reconstruction of sky spherical harmonics coefficients from pure noise visibilities ($\tilde{V}_{ij} = \tilde{n}_{ij}$), the covariance matrix $\mathbf{Cov}(\ell_1, \ell_2)$ of the estimator $\hat{\mathcal{I}}(\ell, m)$ for each mode m can be computed from the \mathbf{L}_m^{-1} matrix and the noise covariance matrix $\mathbf{N}_m = [\tilde{n}_{ij}]_m \cdot [\tilde{n}_{ij}]_m^\dagger$,

$$\mathbf{Cov}_m(\ell_1, \ell_2) = \langle \left[\hat{\mathcal{I}}(\ell) \right]_m \cdot \left[\hat{\mathcal{I}}(\ell) \right]_m^\dagger \rangle = \mathbf{L}_m^{-1} \mathbf{N}_m \mathbf{L}_m^{-1\dagger}$$

The covariance matrix is not diagonal, especially due to partial sky coverage in declination. However, if we ignore this correlation and use the diagonal terms only for each m mode, we can gather them together to create the $\sigma_{\mathcal{I}}^2(\ell, m)$ variance matrix. This matrix informs us on how well each (ℓ, m) mode is measured.

$$\sigma_{\mathcal{I}}^2(\ell, m) = \mathbf{Cov}_m(\ell, \ell) \quad (14)$$

We consider a survey duration of two full years for the results presented in this paper. The total integration time for each visibility time sample would be $t_{int} \sim 2 \times 10^4$ s for $n_t = 2m_{max} = 3000$. Assuming a system temperature $T_{sys} = 50$ K, and $\Delta\nu = 1$ MHz, the effective σ_{noise} for measured visibility time samples can then be written as a function of integration time per time sample t_{int} :

$$\sigma_{noise} = \frac{\sqrt{2}T_{sys}}{\sqrt{t_{int} \Delta\nu}} \sim 0.49 \text{ mK} \quad (15)$$

3 THE REGULAR ARRAY CONFIGURATION

The primary beams for each feed on the cylinders is narrow in the East-West (EW) direction and wide in the North-South (NS) direction, as determined by the cylinder reflector curvatures. We model the primary beam of a single feed on associated with a cylindrical reflector as

$$D(\alpha, \beta) \propto \frac{\sin(\alpha\pi(L_x/\lambda))}{\alpha\pi(L_x/\lambda)} \frac{\sin(\beta\pi(L_y/\lambda))}{\beta\pi(L_y/\lambda)} \quad (16)$$

where (α, β) are the two angles with respect to the feed axis, along the EW and NS planes respectively. λ is the wavelength, L_x and L_y are the effective feed sizes along the EW and NS planes. We take $L_y = 0.3$ m for the Tianlai cylinder feeds, and $L_x = 13.5$ m corresponding to an illumination efficiency of 0.9 for the feed on the 15 m wide cylinder. These parameters gives a beam width $\sim 100^\circ$ in the North-South direction, and $\sim 2^\circ$ in the East-West direction at 750 MHz. The actual values will be obtained by fitting the real observational data, these are heuristic values but should be sufficient for our estimations here. The primary beam is shown as the left panel of Fig. 3.

For uniformly spaced linear arrays, grating lobes appear when the spacing is larger than half wavelength ($d_{sep} > \lambda/2$). This is because the phase factor $\exp(i2\pi d_{sep} \sin \theta/\lambda)$ is periodic with respect to $\sin \theta$, and when $d_{sep} > \lambda/2$ the maximum appears more than once. We show the synthetic beam for the regular case 1 and regular case 2 in the central and right panels respectively in Fig. 3. These are obtained by making the full synthesis of a point source image located at the latitude of the array, i.e. $44^\circ 10'$. As we can see in the figure, there are strong grating lobes along the NS direction in the synthetic beams. The position of the n th order grating lobe is $\sim n\lambda/d_{sep}$. At 750 MHz, the positions are $\pm 57.3^\circ$ for the regular case 1 ($d_{sep} = 0.4$ m) and $\pm 28.6^\circ$ for the regular case 2 ($d_{sep} = 0.8$ m). In addition, there are also primary beam side lobes along both the NS and EW direction, these are less prominent in their level and has smaller periods.

To have a better understanding of the synthetic beams in the spherical harmonic space, let us consider the beams of a single pair of receivers. In Fig.4 we show the beam patterns function for four cases: the auto-correlation (top left), and the cross-correlations for a due EW baseline between two cylinders (top right), for a due NS baseline (bottom left), and a SE-NW baseline (bottom right). By definition, only the region $-\ell < m < \ell$ has valid values. In the dish case (see paper I), the autocorrelation covers a triangular region with the top at the origin $(\ell, m) = (0, 0)$, two sides and extends along $m = \pm \ell \cos \delta$ where δ is declination of the observation, and up to $\ell_{max} = 2\pi D/\lambda$ where D is the effective aperture. The auto-correlation in the cylinder case is very different, taking up a butterfly shape. This is because the cylinder primary beam is asymmetric in the NS and EW direction. As described in Eq. (16), along the NS direction which corresponds to $m \sim 0$ the primary beam has very low resolution, while along the EW direction the cylinder primary beam is about $\sim 2^\circ$ at 750 MHz, which corresponds to $\ell \sim 2\pi L_x/\lambda \sim 210$. Indeed, the figure shows that the auto-correlation function extends substantially to

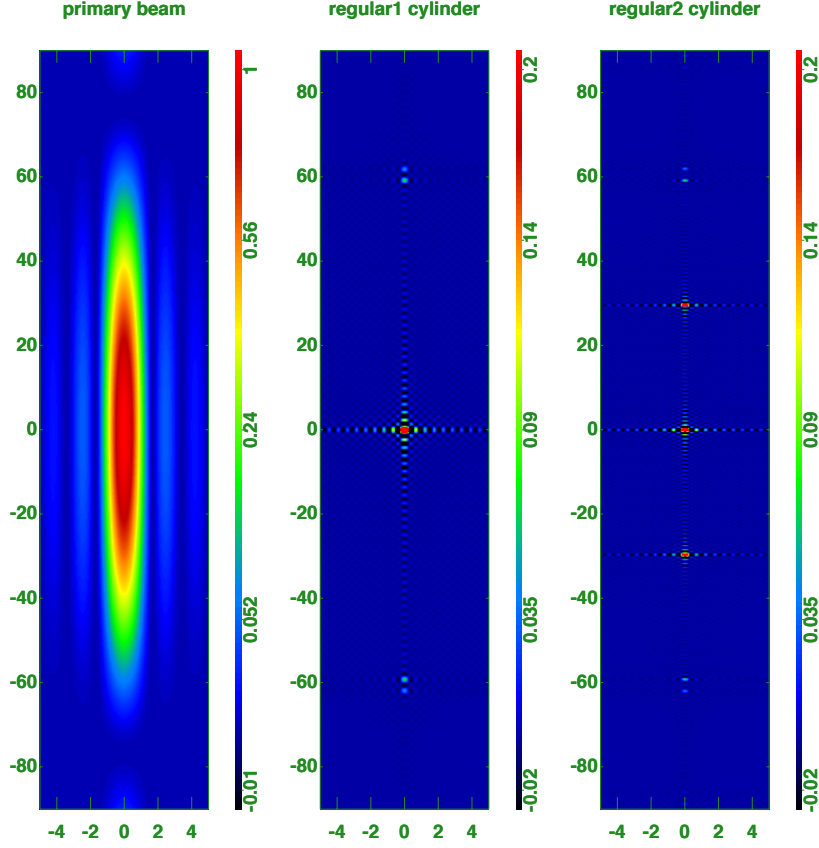


Fig. 3 The primary beam (left) and synthetic beams for the regular 1 (center) and regular 2 (right) configurations.

$\ell \sim 210$ along the two wings. Also, since the cylinder has almost the whole observable sky in its field of view, which includes the equator, the $m = \pm\ell$ is saturated.

For the cross-correlations, the beam pattern centers at $(\ell, m) \sim (2\pi|\mathbf{u}|, 2\pi u)$ as expected, where $\mathbf{u} \equiv (u, v, w) = (b_x, b_y, b_z)/\lambda$. So the EW baseline is centered near $m \sim \ell$, while NS centered near $m = 0$, with $\ell \sim 2\pi b/\lambda$. Note that here we are plotting only positive part of the baseline in one direction, so for the EW baseline the beam is on the $m > 0$ side. If we are to plot the reverse direction, it would appear on the symmetric position at $m < 0$.

Figure 5 shows the response matrix $\mathbf{R}(\ell, m)$ for the two regular configurations at frequency 750MHz. In paper I, we noted that for each baseline the \mathbf{R} matrix has a certain distribution centered at $(\ell, m) = 2\pi b/\lambda$, where b is the baseline length. The m position depends on both the EW component of the baseline and the declination of the strip to be observed. For an array with many baselines the \mathbf{R} matrix are well described by the superposition of these individual baselines. For the cylinder array, the field of view is not limited to a narrow strip, but a hemisphere or even larger spherical zone. As such, the cylinder baseline would only be bounded by $m = \ell$. In the cylinder case, the \mathbf{R} matrix at $m = 0$ is significant up to $\ell \sim 190(380)$ for the Regular 1 (Regular 2) case, which corresponds to the modes probed by the maximum baseline along one cylinder. The longest baseline of the array is however the diagonal ones, i.e. the baselines from North/South end of the East cylinder to the South/North end of the West cylinder, so the \mathbf{R} matrix distributes mostly on a band along $m = \ell$, with some extension to

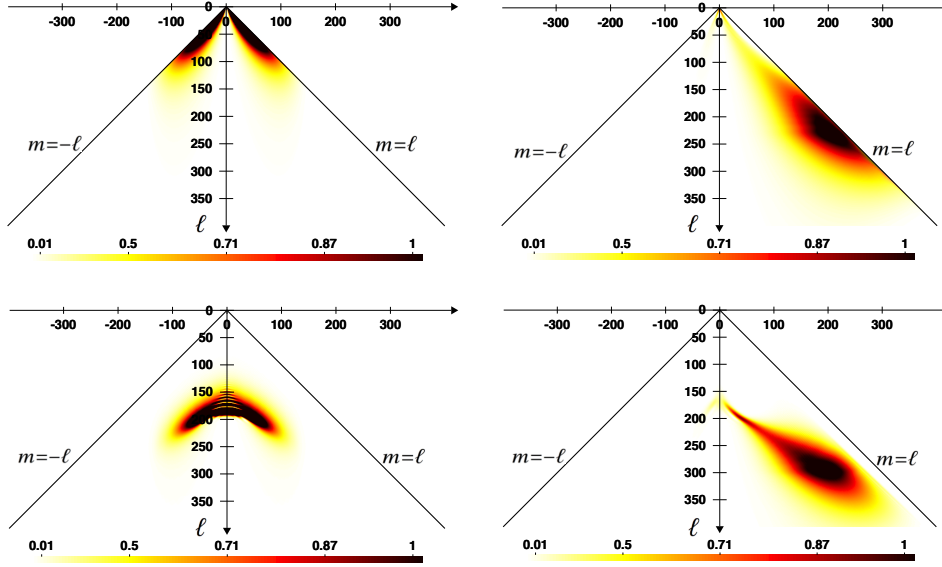


Fig. 4 The beam patterns in spherical harmonics $\mathcal{L}_{\ell,m}$ with size $L_x = 13.5\text{m}$, $L_y = 0.3\text{m}$ and centered at latitude 44.15° . Top Left: auto-correlation of a feed; Top Right: cross-correlation for a EW baseline with $d_{\text{sep}} = 15\text{m}$; Bottom Left: cross-correlation beam for a NS baseline with $d_{\text{sep}} = 12\text{m}$; Bottom Right: cross-correlation for a SE-NW baseline with $(\Delta x, \Delta y) = (15\text{m}, 12\text{m})$.

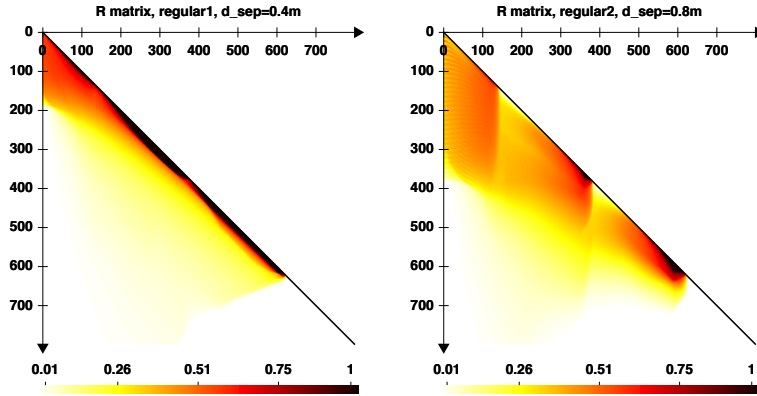


Fig. 5 Comparison of the R matrix for regular 1(left) and regular2 (right) configurations.

higher ℓ in the region between $m = 0$ and $m = \ell$, forming a shark fin shape. The region near $m \sim 0$ is limited to relatively small ℓ due to the fact that our NS baselines are shorter, especially for the Regular 1 case. Future extensions which fill up the remaining part of the cylinder would help improve the $m = 0$ region. In the Regular 2 case, larger part of the (ℓ, m) space are covered than the Regular 1 case, but here the receivers are spread more widely, reducing the density of the baseline coverage, so here there are more apparent non-uniformity, as shown by the vertical stripes at $m = 120$ and 350 . These can be

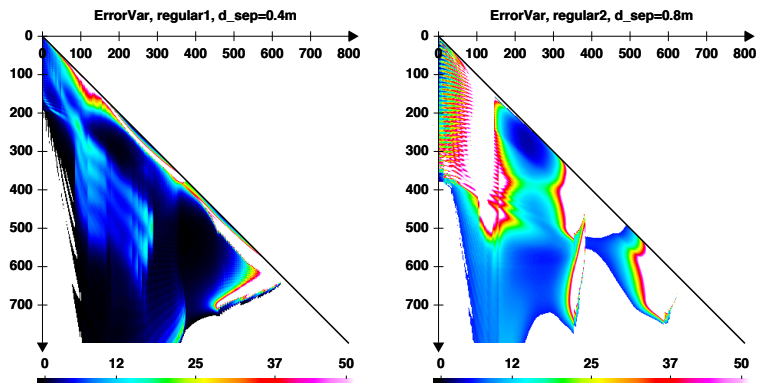


Fig. 6 Comparison of the error variance matrix for regular 1(left) and irregular2 (right) configurations.

understood as follows: as shown in Fig.4, each baseline is sensitive to some part of the (ℓ, m) space. The part of (ℓ, m) space which is not covered by baselines in the array would not be well reconstructed. As the cylinder array are aligned along the three cylinders, we can expect that the m value centered at 0, 235, 470 will be covered, while regions between these, centered at $m = 120$ and 350 are not well covered and may have large errors. Furthermore, if looking carefully, some fringes near $m = 0$ can also be seen, which may be due to the grating lobes.

Figure 6 shows the corresponding error covariance matrix in the (ℓ, m) basis at 750 MHz. For the Regular 2 case the error is particularly large, but even for the Regular 1 case, the errors are also relatively large at these m values. The error values at other regions are relatively small. Additionally, in the Regular 2 case, near $m = 0$ there is relatively large error and also the error shows some rapid modulation in ℓ . These fringes are similar to the ones appeared in the \mathbf{R} matrix at the same positions, and are due to the strong grating lobes.

In Fig.7 we show the reconstructed map at 750MHz derived from simulated regular cylinder array observation ignoring the instrument noise. The top figure use the Regular 1 configuration, and the bottom figure use the Regular 2 configuration. Comparing with the original map Fig. 2, there are spurious features appearing in the reconstructed map. This is very obvious for the Regular 2 case, and also present in the Regular 1 case (e.g. the bright spot at $(270^\circ, 54^\circ)$). These are produced by the grating lobes of the brighter sources such as the Galactic plane and strong point sources, and the Regular 2 case is worse than the Regular case 1. Because of such spurious features, one can not use array with such configurations to make reliable sky survey.

4 THE IRREGULAR ARRAY CONFIGURATION

As we saw in the last section, spurious images appeared in the reconstructed maps of the regular array due to the presence of grating lobes. To avoid this problem, one could adopt spacings less than half wavelength, or employ non-uniform spacing in the linear array. However, at the wavelength of our observation, it is not practical to have spacing less than half wavelength. There are many possible non-uniform spacing schemes, here we choose a very simple one: adopting slightly different spacings on the three different cylinders. So we take the same total length on the three cylinders, but place 31, 32, and 33 feeds on each cylinder, so that the unit separations are different in each case. We choose the same two total lengths as the regular cases described in last section. So for the Irregular 1 case, the basic spacings are $d_{\text{sep}} = 0.413, 0.4, 0.388\text{m}$ for the three cylinders respectively, with a total length of 12.4m; for the Irregular 2 case, the basic spacings are 0.827, 0.8 and 0.775 m respectively, with a total length of 24.8m.

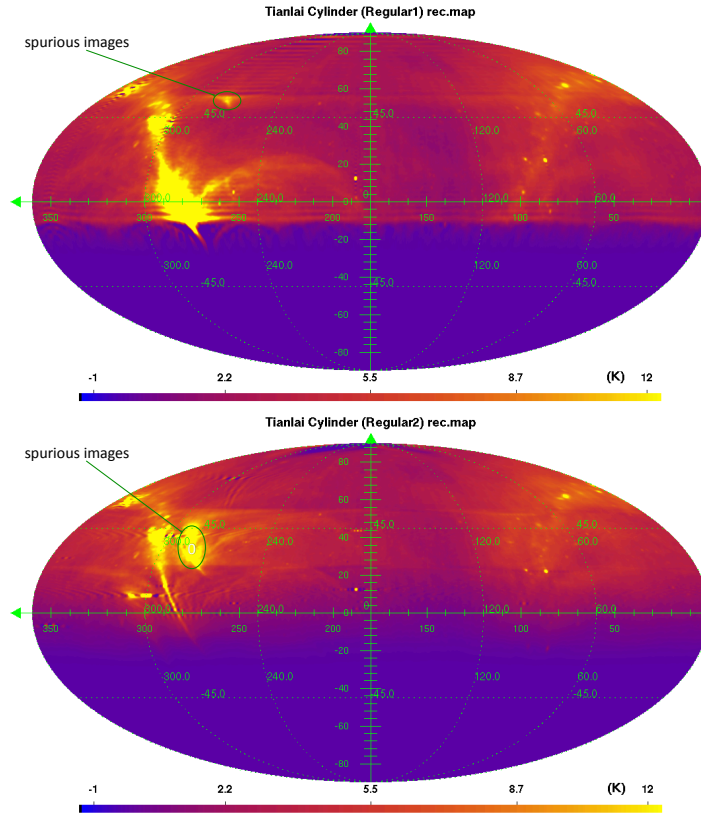


Fig. 7 Reconstructed sky map for the Tianlai cylinder configuration at 750 MHz. Top: Regular 2 configuration; Bottom: Regular 1 configuration. The input map is the GSM map at 750 MHz.

There are still some degeneracies in the north-south baseline. For instance, there are 30, 31, 32 instances of $d_{\text{sep}} = 0.413, 0.4, 0.388\text{m}$ NS baselines in the Irregular 1 configuration, respectively. Nevertheless, for the whole array there are NS baselines of different lengths. The slightly different positioning of the receivers also creates baselines which deviates from the EW direction to different degrees. The whole set up allows wider and more uniform coverage on the (ℓ, m) -plane.

Fig. 8 shows the synthesized beam for the two irregular cases. Here we see that the level of grating lobes is greatly reduced. Whereas in Fig.3 we can see clearly the sharp grating lobes at 28° for Regular 2 configuration and at 57° for both Regular 1 and Regular 2 configurations, in Fig. 8 at these angles the lobes are barely visible. Of course, there are still the primary beam side lobes, but these are generally much smaller. Here we note that the Irregular 2 lobes are weaker than the Irregular 1 lobes.

We plot in Figure 9 the compressed response matrix $\mathbf{R}(\ell, m)$ for the Irregular1 (left) and Irregular2 (right) configurations at 750MHz. As expected, the general shapes of the (ℓ, m) space distribution are similar for the two cases, but with a wider area covered in the (ℓ, m) space for the Irregular 2 configuration due to the larger array sizes. The broad outline of the shapes in this figure are also similar to those in Fig.5, but here the distribution is more smooth and uniform due to the more widely spread-out (ℓ, m) coverage in the irregular configurations. The features at $m = 120$ and 350 in Irregular 2 configuration are much less prominent than in the Regular 2 case.

Figure 10 shows the corresponding error covariance matrix in the (ℓ, m) basis. Here the regions of larger error are spread out more widely, but the error value at the maximum is much reduced when

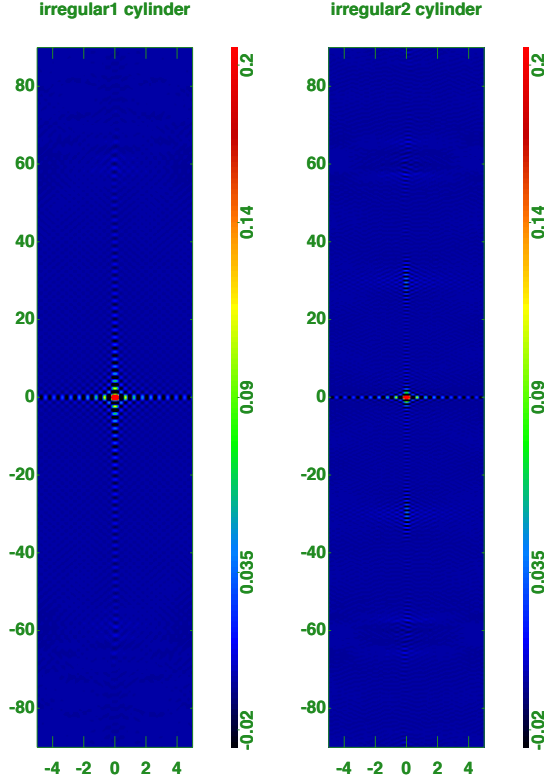


Fig. 8 The synthetic beam for Tianlai cylinder irregular configuration.

compared with the regular configurations. The Irregular 1 case has smaller errors than the Irregular 2 case, as the baselines are more concentrated in the former case which helps reducing the errors.

Figure 11 shows the simulated reconstruction map at 750 MHz with the Irregular 1 (top) and Irregular 2 (bottom) configurations. We can see that in both cases, the reconstruction works relatively well, the spurious features shown in Fig.7 are absent in these figures, and most features of the original map are well produced. There are still some regions where the reconstruction shows some artefacts, e.g. the stripes at $(350^\circ, 60^\circ)$ and $(190^\circ, 12^\circ)$ in the Irregular 1 map, and the stripes south of the equator in the Irregular 2 map. However, the overall quality for the two maps are good.

In Figure 12, we plot the power spectrum transfer functions $T(\ell)$ (left panel) and the noise power spectrum (right panel) for the Irregular 1 and Irregular 2 configurations. Here we have masked out the border pixels outside the band $0^\circ < \theta < 105^\circ$ which are not well constructed, and suppressed (ℓ, m) modes with large errors by applying a weight proportional $\sigma_{\mathcal{I}}^{-2}(\ell, m)$ to all modes which have error larger than $K\sigma_{min}^2$, where σ_{min} is the minimum value of the noise covariance matrix, and for the threshold value we choose $K = 50$. The transfer function decreases toward higher ℓ , but it is generally smooth, though there are curvatures at certain ℓ s. The Irregular 1 configuration has higher response at lower ℓ , but decreases more rapidly at higher ℓ as expected, as its baselines are concentrated in smaller regions and sensitive more to the larger angular scales. For the noise power spectrum, we see that the Irregular 1 configuration achieved lower noise power than the Irregular 2 configuration. In both cases the noise power spectrum show several peaks and troughs, which are due to the different density of baselines on the (ℓ, m) plane. We also draw the expected large scale structure 21cm signal power on the same plot, where we assume cosmology from (Planck Collaboration et al. 2014), and for neutral hydrogen we adopt $\Omega_{HI}b = 0.62 \times 10^{-3}$ (Switzer et al. 2013). The 21cm signal is only a few times the

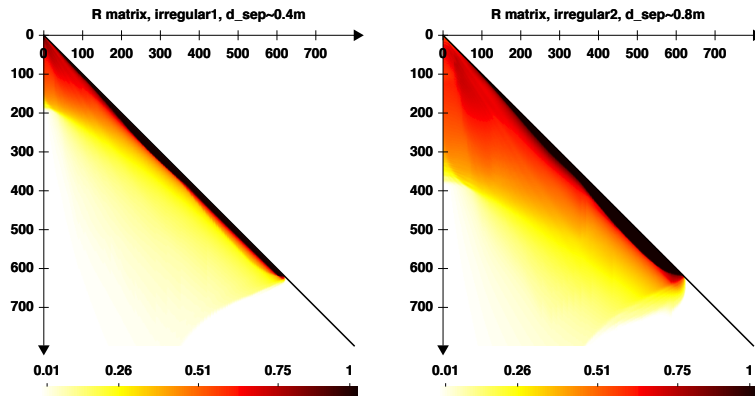


Fig. 9 Comparison of the R matrix for the Irregular 1 (left) and Irregular2 (right) configurations.

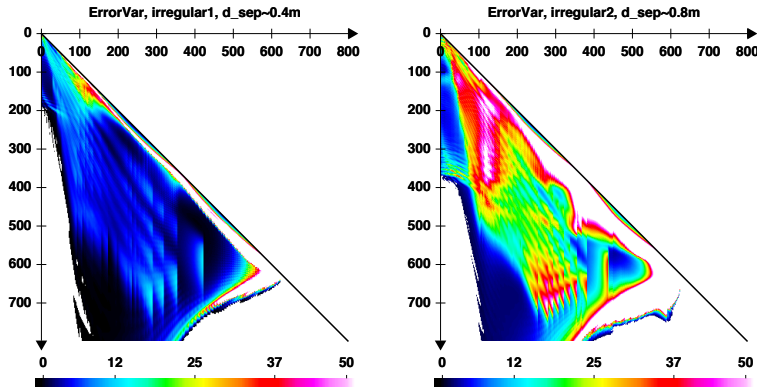


Fig. 10 Comparison of the error variance matrix for irregular configurations.

noise. Note that this is for the detection at a single frequency, we will have more frequency data, but at the same time there are also complications of foreground removal and calibration, which are beyond the scope of the present work. Considering these factors, we see that detecting the 21cm signal would be a great challenge.

5 CONCLUSION

The Tianlai experiment aims to make a low angular resolution, large sky area transit survey of the large scale structure by observing the redshifted 21cm line from neutral hydrogens. By adopting the transit survey strategy, where the telescope is fixed on the ground and scans the whole observable part of sky by the rotation of sky, the cost for building the telescope is reduced, and the instrument is also more stable. The transit scan is however very different from the tracking observation, and for the whole sky survey one must also take into account the sphericity of the sky.

We have developed an efficient, flexible and parallel code to make sky map from transit visibilities based on spherical harmonics transformations, which is applicable to any transit-type interferometer. This paper is the second of a series of papers presenting our transit array data processing method. In this paper, we have applied this software to the simulation of map-making process for the Tianlai cylinder

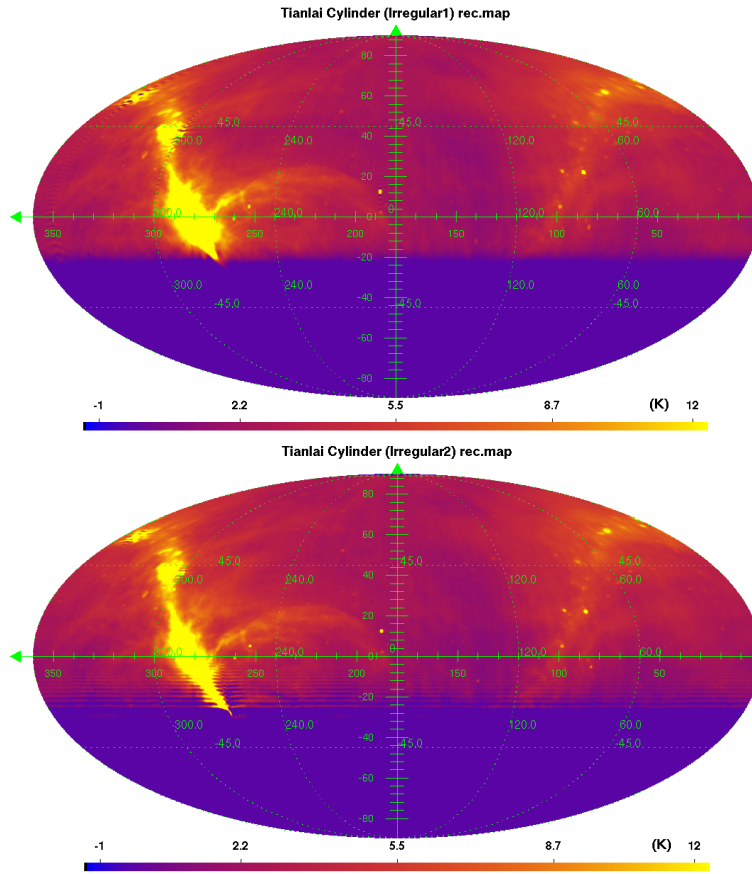


Fig. 11 Reconstructed sky map for the Irregular 1 (top) and Irregular 2 (bottom) configurations at 750 MHz.

array pathfinder. In the simulation, we first compute the visibility time streams for several instrument configurations and scan strategies, and then reconstructed sky maps from these visibilities. The feed response and array geometry are assumed to be known and fully calibrated.

The Tianlai pathfinder have 96 receiver feeds in total, averaging 32 on each cylinder. The cylinders could host about twice that amount of receiver feeds, leaving room for upgrading in the future after the present hardware designed is checked out thoroughly in experiment. We considered two types of arrangement of the feeds. In one type, the feeds are spaced at about one wavelength, which covers less than half of the cylinder length with the 32 feeds on each. In the other type, $3/5$ of the cylinder length is covered, with spacing of twice the wavelength.

On each cylinder the receiver feeds form regularly spaced linear arrays, which have grating lobes if the unit spacing is larger than half wavelength. Coupled with the large instantaneous field of view for the cylinder, the grating lobes could be a great obstacle for map-making. To solve this problem, irregular spacing can be introduced. A logistically simple solution is to adopt slightly different unit spacings on the three cylinders, but on each cylinder the spacing is still uniform. We considered the arrangement of 31, 32, and 33 feeds on the three cylinders. With such irregular configurations, the grating lobes are reduced to very low level, and map reconstruction quality is enhanced.

We analysed the beams produced by the cylinders, and found that the features in the response matrix and noise variance matrix can be understood from these. We also computed the transfer function, and

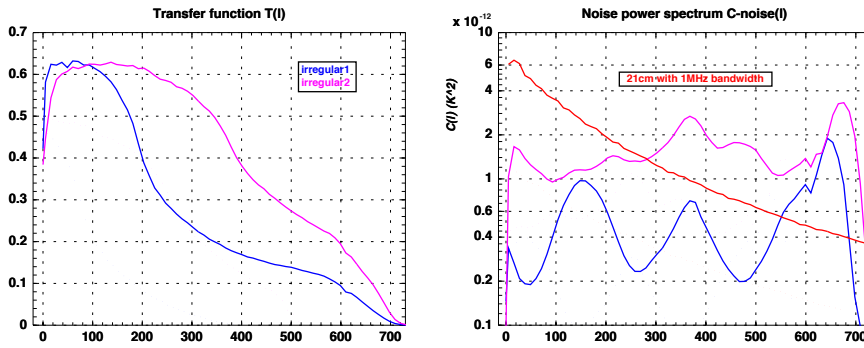


Fig. 12 Comparison of the transfer function $T(\ell)$ (left panel) and the noise power spectrum $C^{\text{noise}}(\ell)$ (right panel) for the Irregular 1 and Irregular 2 configurations.

reconstructed map for both the Regular and Irregular instrument configurations. We also computed the noise angular power spectrum, which determines the array sensitivity for cosmological 21 cm signal measurement. This may be regarded as a simplification of the real case, where the system temperature is dominated by the foreground radiation. We found that for a system temperature of 50 K, the 21cm angular power spectrum is a few times of the noise power in a single 1MHz narrow band. Detecting such signal would be a difficult challenge, but the signal may be enhanced by considering joint measurement of the power spectrum over many spectral bins. In the present paper we study primarily the foreground map-making process, the calibration, foreground removal and 21cm signal extraction will be investigated in subsequent works.

ACKNOWLEDGEMENTS

We would like to thank Ue-Li Pen and Richard Shaw for discussions. The Tianlai project is supported by the MoST 863 program grant 2012AA121701 and the CAS Repair and Procurement grant. PAON4 project is supported by PNCG, Observatoire de Paris, Irfu/CEA and LAL/CNRS. JZ was supported by China Scholarship Council. XC is supported by the CAS strategic Priority Research Program XDB09020301, and NSFC grant 11373030. FW is supported by NSFC grant 11473044.

References

- Ansari, R., et al. 2009, arXiv:0807.3614
 Ansari, R., Campagne, J. E., Colom, P., et al. 2012, *A&A*, 540, A129
 Bandura, K., Addison, G. E., Amiri, M., et al. 2014, in *Society of Photo-Optical Instrumentation Engineers (SPIE) Conference Series*, Vol. 9145, Society of Photo-Optical Instrumentation Engineers (SPIE) Conference Series, 914522
 Barata, J. C. A., & Hussein, M. S. 2012, *Brazilian Journal of Physics*, 42, 146
 Battye, R. A., Browne, I. W. A., Dickinson, C., et al. 2013, *MNRAS*, 434, 1239
 Chang, T.-C., Pen, U.-L., Peterson, J. B., & McDonald, P. 2008, *Physical Review Letters*, 100, 091303
 Chen, X. 2012, *International Journal of Modern Physics Conference Series*, 12, 256
 Chen, X. 2015, *IAU General Assembly*, 22, 2252187
 Connor, L., Lin, H.-H., Masui, K., et al. 2016, arXiv:1602.07292
 de Oliveira-Costa, A., Tegmark, M., Gaensler, B. M., et al. 2008, *MNRAS*, 388, 247
 Feng, L., Vaulin, R., & Hewitt, J. N. 2014, arXiv:1405.6219
 Gong, Y., Chen, X., Silva, M., Cooray, A., & Santos, M. G. 2011, *ApJ*, 740, L20
 Górski, K. M., Hivon, E., Banday, A. J., et al. 2005, *ApJ*, 622, 759
 Masui, K., Lin, H.-H., Sievers, J., et al. 2015, *Nature*, 528, 523

- Peterson, J. B., Bandura, K., & Pen, U. L. 2006, astro-ph/0606104
- Planck Collaboration, Ade, P. A. R., Aghanim, N., et al. 2014, A&A, 571, A16
- Seo, H.-J., Dodelson, S., Marriner, J., et al. 2010, ApJ, 721, 164
- Shaw, J. R., Sigurdson, K., Pen, U.-L., Stebbins, A., & Sitwell, M. 2014, ApJ, 781, 57
- Switzer, E. R., Masui, K. W., Bandura, K., et al. 2013, MNRAS, 434, L46
- Xu, Y., Wang, X., & Chen, X. 2015, ApJ, 798, 40
- Yu, H.-R., Zhang, T.-J., & Pen, U.-L. 2014, Physical Review Letters, 113, 041303
- Zhang, J., Ansari, R., Chen, X., et al. 2016, arXiv:1606.03090